INSTITUTE OF PHYSICS PUBLISHING and INTERNATIONAL ATOMIC ENERGY AGENCY NUCLEAR FUSION

Nucl. Fusion **44** (2004) 533–541 PII: S0029-5515(04)77326-3

Confinement and transport in EC heated RI-mode discharges in TEXTOR

G.M.D. Hogeweij[1], P. Dumortier[2], D. Van Eester[2], F.A. Hoekzema[3], R.J.E. Jaspers[1], D. Kalupin[3], H.R. Koslowski[3], A. Messiaen[2], R.W. Polman[1], F.C. Schüller[1], B. Unterberg[3], M. Vervier[2], G. Van Wassenhove[2] and E. Westerhof[1]

[1] FOM-Institute for Plasma Physics Rijnhuizen, Association EURATOM-FOM, PO Box 1207, NL-3430 BE Nieuwegein, The Netherlands[a]

[2] Laboratoire de Physique des Plasmas-Laboratorium voor Plasmafysica, Association EURATOM-Belgian State, ERM/KMS, Brussels, Belgium[a]

[3] Institut für Plasmaphysik, FZ Jülich GmbH, EURATOM Ass., D-52425 Jülich, Germany[a]

Received 17 October 2003, accepted for publication 4 March 2004
Published 26 March 2004
Online at stacks.iop.org/NF/44/533
DOI: 10.1088/0029-5515/44/4/007

Abstract

This paper reports on experiments in TEXTOR with electron cyclotron resonance heating (ECRH) of radiatively improved (RI) mode discharges. With ECRH the energy content of RI-mode discharges can be increased without the normally observed power degradation in confinement time. The experiments are described and the effects of ECRH on global confinement and local plasma parameters of RI-mode discharges are discussed; the favourable scaling of energy content is due to a zone of low electron thermal transport just outside the sawtooth inversion radius. Moreover, the heating effect of ECRH in the RI-mode is compared with the effect in L-mode; this comparison sheds some light on the physics of electron thermal transport in RI-mode discharges.

PACS numbers: 52.25.Fi, 52.55.Fa, 52.50.Gj

1. Introduction

In TEXTOR a regime with improved confinement, the radiatively improved (RI) mode, has been established by injection of radiating species in the plasma edge (typically Ne or Ar) [1, 2]. Apart from a radiating mantle, this regime is characterized by the establishment of a peaked density profile. The energy confinement in RI-mode scales with line-averaged density ($\bar{n}_e$) as in the linear Ohmic confinement regime; however, the general degradation of confinement with total heating power remains [1]: $\tau_{RI} \sim \bar{n}_e P_{tot}^{-2/3}$. Recently, improvement of confinement with impurity injection has also been obtained at DIII-D, JET and FTU [3–6].

The improvement of confinement is attributed to the suppression of the ion temperature gradient (ITG) turbulence [7], which is believed to be a major cause of anomalous ion heat conductivity. In this respect it should be noted that the RI-mode can be regarded as the high-power counterpart of improved Ohmic confinement (IOC). In high density Ohmic TEXTOR discharges IOC could be triggered by a sudden reduction in the external gas flow, and is characterized by a peaked density profile and suppression of ITG [8]. To complete the picture, roll-over from the RI-mode back to the L-mode can be provoked by a strong gas puff, i.e. by flattening the n_e profile [9].

Electron thermal transport, in particular its behaviour in the RI-mode, is less well known than ion thermal transport. It is, therefore, of particular interest to study the effect of additional electron heating as provided by electron cyclotron resonance heating (ECRH). Therefore, several experiments with ECRH applied in RI-mode discharges have been performed. These experiments are reported in this paper.

This paper is organized as follows. Section 2 describes the ECRH system on TEXTOR and the set-up of the experiments. The next two sections describe the effect of ECRH on global confinement and on local plasma parameters, respectively. Then, section 5 treats the local power balance in ECR heated RI-mode discharges. In section 6 the RI-mode is compared with the L-mode. The results are discussed in section 7.

2. ECRH and experimental set-up

RI-mode discharges are routinely obtained in TEXTOR by first switching on additional heating power, usually both neutral beam injection (NBI) and ion cyclotron resonance heating

[a] Partners in the Trilateral Euregio Cluster.

(ICRH), followed by the injection of neon. The edge of the plasma is strongly cooled by the radiating neon ions, and due to reduction of anomalous transport both the density and, to a lesser extent, the temperature profiles peak.

In the experiments reported here, ECRH was applied in well-established RI-mode discharges, i.e. 1–1.5 s (i.e. ∼20–30 energy confinement times) after the start of neon injection.

For the experiments, one 110 GHz gyrotron was used, pulse length 200 ms, delivering into the plasma effectively 270 ± 30 kW in the second harmonic X-mode. Heating is from the low field side. The launcher used with the 110 GHz gyrotron consists of a fixed focusing mirror (copper) and a steerable flat mirror (stainless steel). The steerable mirror can be rotated around a vertical axis to choose the angle of injection in the toroidal direction between -45° and $+45^\circ$, and thus to drive current. It can also be rotated around a horizontal axis (between -15° and $+15^\circ$, which means that the beam injection angle varies between -30° and $+30^\circ$) to cover the poloidal cross-section.

Unfortunately, the 200 ms pulse length and 270 ± 30 kW injected power of the preliminary 110 GHz system are limited when compared to confinement times of about 50 ms and the total heating power of about 2.7 MW of typical RI-mode discharges. Still, interesting results have been obtained on ECRH in the RI-mode.

3. Effect of ECRH on global confinement

ECRH with central resonance ($B_t \simeq 2.08$ T) was applied to RI-mode discharges in TEXTOR at several values of plasma current ($300 \leqslant I_p$ [kA] $\leqslant 450$) and line-integrated densities ($3 \leqslant \bar{n}_e$ [10^{19} m^{-3}] $\leqslant 6.5$). Results for a typical RI-mode discharge with central ECRH are shown in figure 1, which gives the time evolution of the various input powers, the total heating power and the diamagnetic energy W_{dia}. During ECRH the density continues to rise: no density pump-out is observed during ECRH in the RI-mode.

We compare the performance with and without ECRH using the RI-mode scaling:

$$\tau_{RI} = 0.18 \cdot \bar{n}_e \cdot P_{tot}^{-2/3} \tag{1}$$

with τ_{RI}, $\bar{n}_e$ and P_{tot} in s, 10^{20} m^{-3} and MW, respectively [1]. For completeness, the performance with and without ECRH will also be compared with the ELM-free H-mode (ITER-93H) scaling, τ_{93H}, defined as [10]

$$\tau_{93H} = 0.036 \cdot I_p^{1.06} B_t^{0.32} \kappa^{0.66} R^{1.90} a^{-0.11} \bar{n}_e^{0.17} M_{eff}^{0.41} P_{tot}^{-0.67} \tag{2}$$

The energy content expected on the basis of these scalings will be denoted by W_{RI} and W_{93H}, and is given in figure 1 as well. As $P_{ECRH}/P_{tot} \simeq 0.27/2.7 \simeq 10\%$ (in fact even less, since P_Ω drops during ECRH), equation (1) would predict a relative increase of stored energy (δW_{dia}) of typically 3%. However, in the discharge shown in figure 1, like in many other well-performing RI-mode discharges, $\delta W_{dia}/W_{dia} \simeq 9\%$ is observed, i.e. with ECRH the energy content of the RI-mode discharges can be increased without power degradation. The difference in time evolution of the two scalings is caused by the difference in density scaling: the RI-mode scaling has a much stronger positive density dependence than the ITER-93H scaling.

In ≃10 discharges P_{ICRH} was under feedback of a preset value of W_{dia}. In this way the effectiveness of ECRH could be compared directly with that of ICRH. In those discharges 270 kW of ECRH was as effective as 500 kW of ICRH, thus confirming the performance improvement (compared to standard scaling laws) during ECRH (see figure 2 for example). It should be noted, however, that the value of B_t was lower than the optimum value for central ICRH resonance.

In figure 3 the normalized efficacy of ECRH, defined as $(\delta W_{dia}/W_{dia})/(\delta P_{tot}/P_{tot})$, is plotted for a number of discharges. The high normalized efficacy of ECRH (close to 1) is seen to hold, up to $\bar{n}_e \simeq 5.5 \times 10^{19}$ m^{-3}. Abel

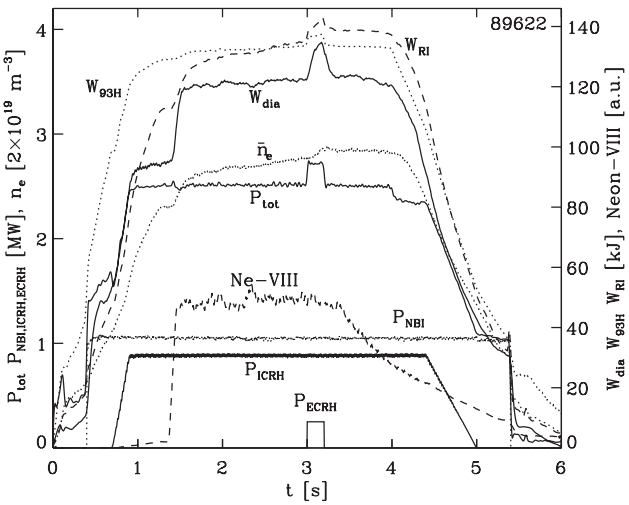

Figure 1. Time traces of line-averaged density ($\bar{n}_e$) and input powers (P_{tot}, P_{NBI}, P_{ICRH}, P_{ECRH}) in units of 2×10^{19} m^{-3} and MW, respectively (left axis), and of W_{dia}, W_{RI} and W_{93H} (kJ, right axis) and neon-VIII line intensity (a.u.) for discharge 89622. Plasma parameters: $I_p = 400$ kA, $B_t = 2.08$ T.

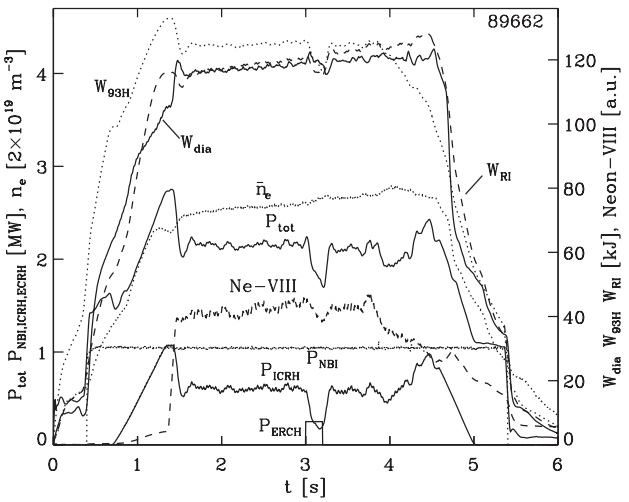

Figure 2. Discharge 89662, where P_{ICRH} was under feedback of W_{dia} (feedback value 120 kJ). The signals with the same scalings as in figure 1 are shown. The positive and negative spike on W_{dia} immediately after switch-on and switch-off of ECRH, respectively, are caused by the slow reaction of the feedback system on the ICRH power. Plasma parameters as in figure 1.

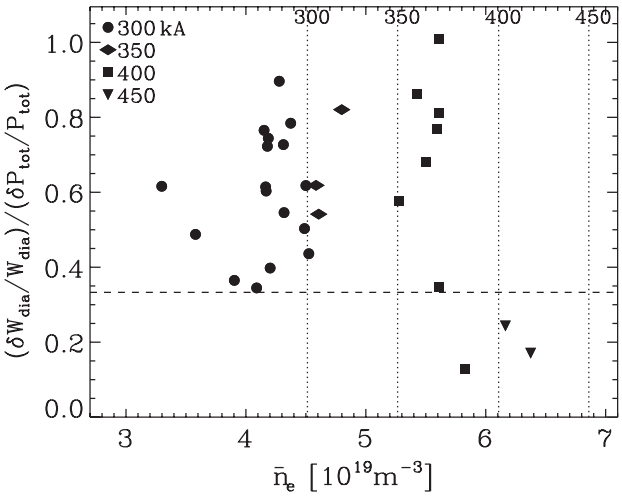

Figure 3. The normalized efficacy of ECRH in RI-mode discharges. The different symbols indicate the plasma current. The dashed line is the normalized efficacy expected by the RI-mode scaling law. The vertical dashed lines indicate the Greenwald density for the four different values of the plasma current. The sharp drop of normalized efficacy near $\bar{n}_e \approx 5.5 \times 10^{19}$ m^{-3} is not caused by the Greenwald density limit but is due to the density becoming higher than the cut-off density for 110 GHz.

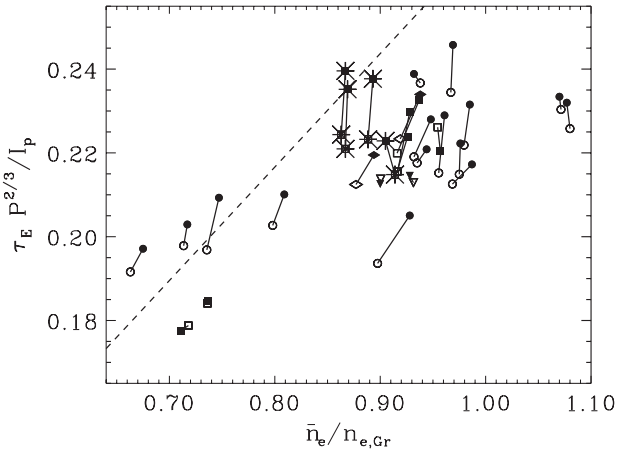

Figure 4. Plot of $\tau_E P_{tot}^{2/3}/I_p$ versus normalized density for the discharges of figure 3. Closed (open) symbols: phase with (without) ECRH. Symbols as in figure 3. The four discharges with P_{ICRH} under feedback are marked with a large asterisk. The standard RI-mode scaling, equation (1), is given by a dashed line.

inversion of the interferometry data shows that this corresponds to $n_e(0) \simeq 7.5 \times 10^{19}$ m^{-3}, coinciding within measurement accuracy with the 110 GHz X-mode cut-off density ($n_{c.o.}^{110,X}$). There is a considerable scatter on the data points in figure 3: the normalized efficacy of ECRH critically depends on the details of the machine condition; the details of this are still not understood. In comparable L-mode discharges (not shown in this plot), the increase of W_{dia} was close to the expected 3%.

The radiation temperatures measured with the central ECE channels start decreasing when $\bar{n}_e$ rises above $\simeq$4.3. The fact that the effectiveness of ECRH is much less affected by the approach of the density cut-off than ECE can be understood by the differences in antenna patterns of the ECE and ECRH systems: whereas the ECRH wave beam is well focused inside the plasma, the ECE antenna pattern has a divergence of 12.5% ($1/e$ half-width of the intensity). Ray tracing calculations from TORAY [11] and NOTEC [12] confirm that the ECRH power deposition profile is practically constant, virtually up to $n_{c.o.}^{110,X}$, while the radiation temperature in the 109 and 112 GHz central ECE channels starts decreasing already at $n_e(0) \geqslant 6.5 \times 10^{19}$ m^{-3}.

Above $n_{c.o.}^{110,X}$ the normalized efficacy of ECRH decreases below 0.2. As the O-mode power is not affected by this cut-off, discharges with central density above $n_{c.o.}^{110,X}$ can, in principle, be heated by injecting O-mode ECRH power. However, the first pass absorption of the second harmonic O-mode is estimated to be only $\simeq$45% at the given plasma parameters, in contrast to nearly 100% single pass absorption of the second harmonic X-mode (below $n_{c.o.}^{110,X}$). In a few RI-mode discharges with density above $n_{c.o.}^{110,X}$, O-mode heating this was tried, yielding a normalized efficacy of $\simeq$0.6, in reasonable agreement with the estimated first pass absorption.

The performance of the ECR heated RI-mode discharges can be appreciated in the diagram of $\tau_E P_{tot}^{2/3}/I_p$ versus $n_e/n_{e,Gr}$, where $n_{e,Gr} = I_p/(\pi a^2)$ is the Greenwald density. The RI-mode scaling shows up as a straight line in this diagram. In figure 4, a number of discharges are shown in this way. Each discharge is represented by two points: one for the average performance during ECRH, and one for the RI-phase without ECRH; the latter is the average value of the phase just before switch-on of ECRH and after switch-off of ECRH (in order to get rid of possible slow trends in the time traces, e.g. a slow density increase during the discharge). There is a small but striking performance improvement (compared to standard scaling laws) during ECRH.

4. Effect of ECRH on local plasma parameters

In this section, the effect of ECRH on local plasma parameters and on the sawtooth behaviour will be analysed.

First, we compare profiles without and with ECRH. Figure 5(a) compares T_e and n_e profiles measured with Thomson scattering (TS) from two similar RI-mode discharges, one with and one without ECRH (thick full and thick dashed line, respectively). Both TS profiles were taken just before a sawtooth crash. For comparison, the T_e and n_e profiles from two L-mode discharges with similar plasma parameters are also shown (thin full and thin dashed lines for cases with and without ECRH, respectively). Unfortunately, the TS profiles in the two L-mode cases were taken just after a sawtooth crash. Therefore, to make a fair comparison, the T_e profiles just before the sawtooth crash were reconstructed from the measured TS T_e profiles using the ECE T_e time traces. Since the n_e profile is quite flat in the core of L-mode discharges, no correction in the measured n_e profiles was needed.

The RI-mode cases have much more peaked n_e compared to the L-mode ones; the peaking is not changed during ECRH. Application of central ECRH in the RI-mode causes a much stronger peaking of T_e than in the L-mode. The example shown here is at relatively modest I_p (300 kA) and $\bar{n}_e$ (4.0×10^{19} m^{-3}); however, the same behaviour is observed at higher I_p and n_e.

In figure 5(b) profiles of T_i and toroidal rotation (v_{tor}), as measured by charge exchange spectroscopy (CXS), are plotted

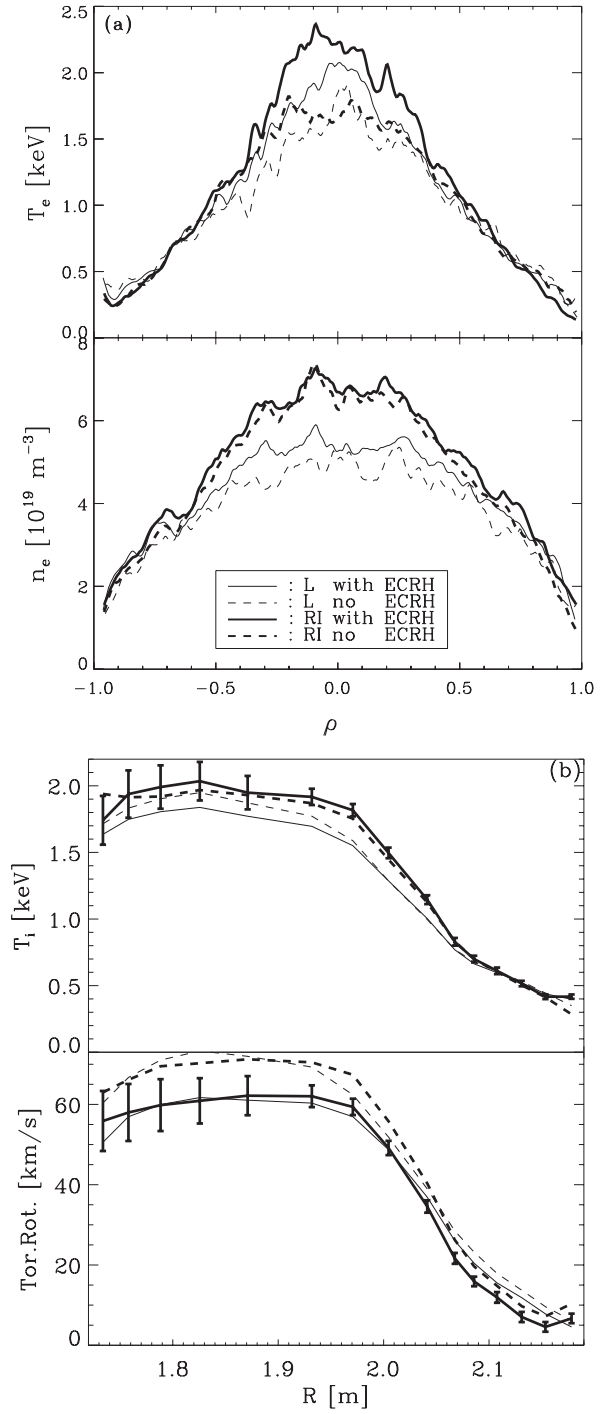

Figure 5. (*a*) T_e and n_e as measured by TS of four discharges at 300 kA, just before the sawtooth crash: L-mode with/without ECRH (discharges 87822/88540, full/dashed thin lines), and RI-mode with/without ECRH (discharges 87823/87826, full/dashed thick lines). Plasma parameters: $I_p = 300$ kA, $B_t = 2.08$ T, $\bar{n}_e = 4.0 \times 10^{19}$ m^{-3}. (*b*) Profiles of T_i and v_{tor} as measured by CXS of L-mode discharge 89621 (thin lines) and RI-mode discharge 89622 (thick lines), both in the phase with and without ECRH (full and dashed lines, respectively). For plasma parameters see figure 1.

for an L-mode and an RI-mode discharge, both for the phase without and with ECRH. Each plotted curve is the average of three CXS measurements, covering 0.15 s. For one or the T_i and v_{tor} profiles the error bars have been plotted as well;

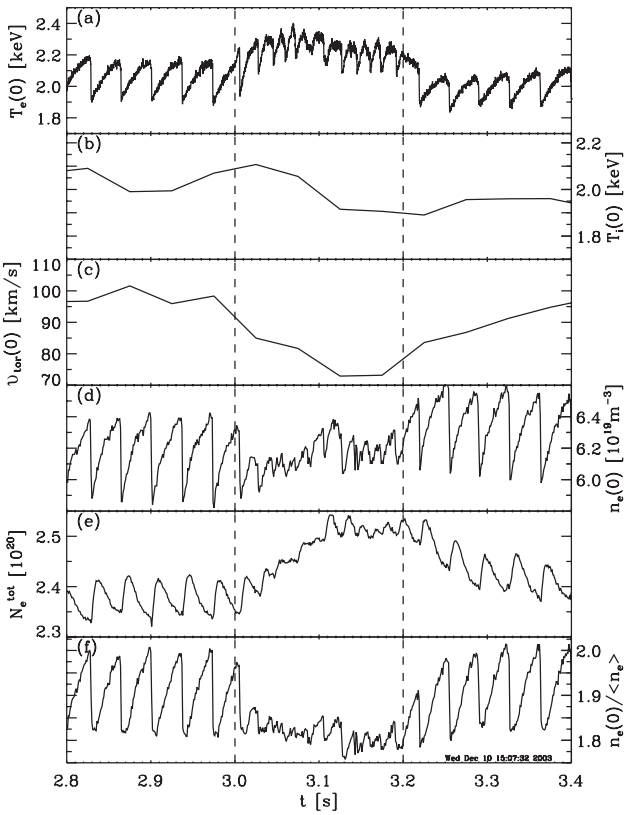

Figure 6. Evolution of plasma parameters during ECRH for RI-mode discharge 89597. Central T_e (*a*), T_i (*b*), v_{tor} (*c*) and n_e (*d*) are shown; moreover, the total number of electrons (*e*) and density peaking factor (*f*) are plotted. Plasma parameters: $I_p = 300$ kA, $B_t = 2.08$ T. Note the strong decrease of v_{tor} during ECRH. There is no sign of density pump-out during ECRH (the total number of electrons even slightly increases). The density profile slightly flattens during ECRH; due to this flattening, the sawteeth are nearly invisible on the central density during ECRH.

the error bars for the other curves are very similar. In the RI-mode T_i is seen to be slightly higher than in the L-mode; this difference is enhanced during ECRH, although the difference is still only marginally outside the error bars. Most striking, however, is the significant decrease of v_{tor} during ECRH, both in L- and RI-mode.

In other experiments, e.g. in DIII-D negative central shear discharges, a strong decrease of both T_i and v_{tor} was observed when strong electron heating was applied [13]; there, a direct relation of this decrease with the ratio T_e/T_i was demonstrated. In DIII-D, however, the electron–ion coupling was much weaker than in the RI-mode discharges in TEXTOR, due to the much lower density and higher T_e in DIII-D; this could mask a possible increase of thermal ion transport during ECRH in TEXTOR RI-mode discharges.

Figure 6 shows the evolution of plasma parameters during ECRH for RI-mode discharge 89597. For this plot a discharge at low n_e was chosen, in order to have the ECE T_e measurements available; however, this plot is indicative of the evolution seen at higher n_e. Most striking is the strong decrease of v_{tor} during ECRH, even stronger than in figure 5(*b*). There is no sign of density pump-out during ECRH, as is normally observed when ECRH is applied in Ohmically heated or in L-mode discharges. The total number

of electrons, i.e. the volume averaged electron density, even increases slightly. The density profile slightly flattens during ECRH; due to this flattening, the sawteeth are nearly invisible on the central density during ECRH; however, the T_e time trace shows that the sawtooth activity does continue during ECRH. The disappearance of the density sawteeth together with the slight increase of the total number of electrons is indicative of a decrease of inward particle convection in the central area of the discharge only.

5. Local power balance and transport

The contribution of ECRH to the total input power is modest. For discharges like 89622, ECRH only adds $\simeq$9% to the total input power. Nevertheless, due to the excellent localization of ECRH compared to ICRH and NBI, its contribution in the core is much higher. Figure 7(*a*) shows the power densities of ECRH, ICRH and NBI directly or indirectly absorbed by the electrons and the ions for discharge 89622, as calculated by the TORAY and PION codes, respectively [11, 14]. The ICRH waves are for a very small part directly absorbed by the electrons and thermal deuterium ions; the major part is absorbed by the D beam ions and the H minority ions. The H minority ions almost exclusively transfer their energy to the electrons; the D beam ions transfer their energy more or less equally to the electrons and thermal ion population. In figure 7(*a*) only the total (direct plus indirect) absorption is shown; the actual breakdown depends on the concentration of H minority ions, which was assumed to be 3% in the calculations.

Figure 7(*a*) shows that, although the overall contribution of ECRH is modest, its local contribution in the centre is dominant. To further exemplify this, figure 7(*b*) shows the integrated deposited power to the electrons before and during ECRH (full and dashed line, respectively) and to the ions (dashed–dotted line), neglecting the Ohmic power (which is small compared to other sources), again for discharge 89622. Note that only 50% (without ECRH) to 55% (with ECRH) of the total power is deposited inside $\rho = 0.4$; this is due to the poor localization of the NBI power, and is the usual situation, also in L-mode discharges. Figure 7(*b*) also shows the relative increase of integrated deposited power to the electrons due to ECRH; it is more than 100% inside $\rho = 0.15$ (ρ denotes the normalized minor radius), and still more than 50% inside $\rho = 0.4$. This is, however, an upper limit as during ECRH the Ohmic power will decrease. If possible changes in power deposition of ICRH and NBI during ECRH are also taken into account, the error bar on the relative increase of electron heat flux becomes quite significant in the region where a local balance analysis can be done, i.e. outside the sawtooth inversion radius (ρ_{inv}). Therefore, from a direct comparison of the local power balance with and without ECRH it would be hard to reliably judge whether electron thermal transport during ECRH has changed.

For this reason, a different strategy was followed to study local transport: a number of series of similar discharges were made, in which the ECRH power deposition radius (ρ_{dep}) was scanned by tilting the mirror of the ECRH launching system around the horizontal axis. Such scans were made at different plasma conditions. Figure 8 shows the results of two such

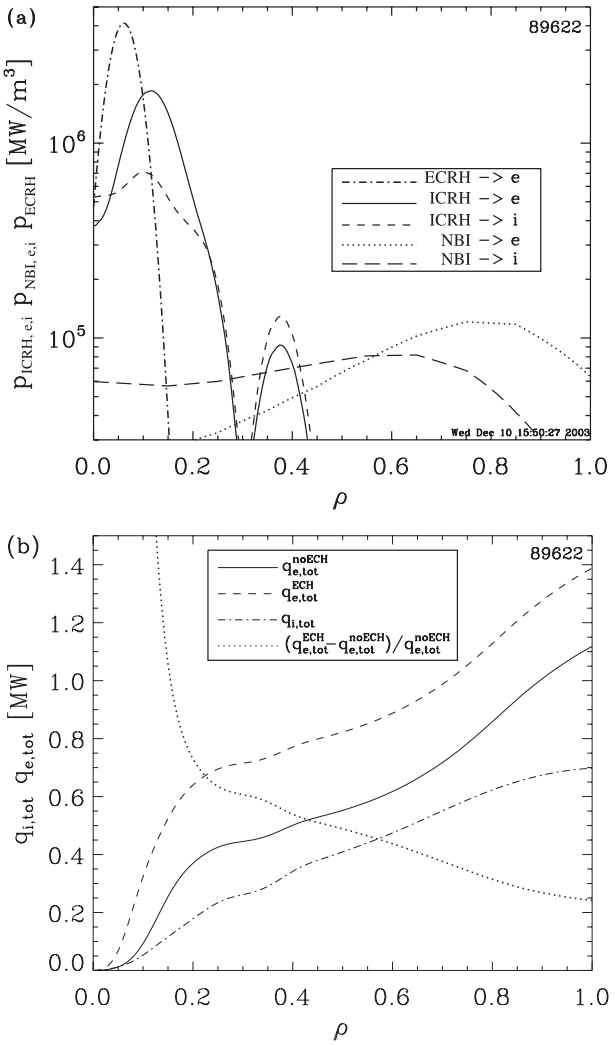

Figure 7. (*a*) Logarithmic plot of the calculated power densities absorbed by the electrons and ions for discharge 89622: ECRH power (fully absorbed by the electrons, — · —); ICRH power (see text) absorbed by the electrons (——) and ions (- - - -); NB power absorbed by the electrons (– – –) and ions (· · · · · ·). In the calculations the parameters of discharge 89622 were used, assuming a H minority concentration of 3%. (*b*) Total electron heat flux neglecting the Ohmic power (full and dashed line before and during ECRH, respectively) and total ion heat flux (— · —). The relative increase of integrated deposited power to the electrons due to ECRH is also shown (· · · · · ·). Outside $\rho \simeq 0.7$ the total heat flux carried by the electrons, $q_{e,tot}$, will be strongly reduced by radiation losses, which have been neglected here.

scans, one at high I_p and $\bar{n}_e$ (400 kA, 5.5×10^{19} m^{-3}) and one at low I_p and $\bar{n}_e$ (300 kA, 4.2×10^{19} m^{-3}). Refraction of the ECRH beam was taken into account in the calculation of ρ_{dep}. For the high I_p case the normalized efficacy of ECRH shows a sharp reduction between $\rho \simeq 0.2$ and 0.4, indicating a local zone of low (electron) heat transport in this region. In the scan at lower I_p the sharp change of normalized efficacy was found to take place in a slightly more inward region, between $\rho \simeq 0.15$ and 0.35. In both scans, the zone of low (electron) heat transport appears to lie near or just outside ρ_{inv}.

Figure 8 also shows the expected normalized efficacy of ECRH as a function of ρ_{dep}. The full line is the case without power degradation ($\chi_{e,i} \sim P^0$); the dashed line is the case

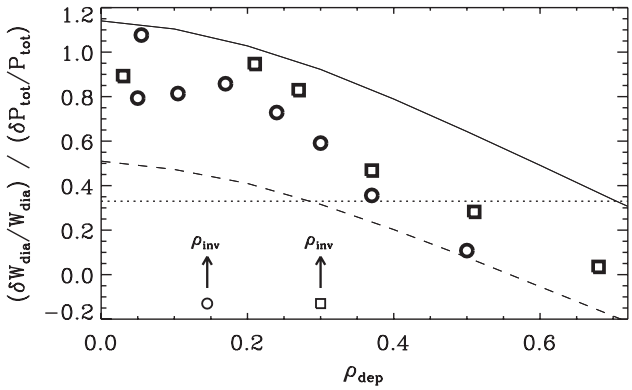

Figure 8. The normalized efficacy $(\delta W_{\rm dia}/W_{\rm dia})/(\delta P/P_{\rm tot})$ from diamagnetic measurements achieved in RI-mode discharges as a function of the normalized ECRH deposition radius. The datasets shown are for $q_{\rm a} = 4.8$ (○) and $q_{\rm a} = 3.6$ (□). The expected efficacy of ECRH without (——) and with (– – –) power degradation are indicated; see text. For both datasets a sharp drop of normalized efficacy is observed close to $\rho_{\rm inv}$ (indicated by arrows), footprint of a transport barrier in that region.

with standard RI-mode power degradation ($\chi_{\rm e,i} \sim P^{2/3}$). For these calculations a parabolic $\chi_{\rm i} = \chi_{\rm e}$ was assumed with $\chi_{\rm e}(0) = 0.6$ and $\chi_{\rm e}(a) = 3.2\,{\rm m^2\,s^{-1}}$; these $\chi_{\rm e,i}$ profiles give a fair reproduction of the experimentally observed $T_{\rm e,i}$ profiles. These simple simulations confirm that ECRH inside $\rho_{\rm inv}$ is much more effective than could be expected on the basis of the RI-mode scaling law.

6. Comparison of the effect of ECRH in L-mode and RI-mode

To further study the different effects of ECRH in L-mode and RI-mode, a neon scan was performed: in five discharges the level of neon puffing was increased from 0 (L-mode) to the highest possible level (i.e. staying just below the density limit); in this way a gradual transition from an L-mode discharge to an RI-mode discharge was obtained. Figure 9 shows time traces of these five discharges. Discharge (a) is an L-mode case (no neon puff); (b) is a weak RI-mode; (c), (d) and (e) are well-developed RI-mode cases. The increase of $W_{\rm dia}$ some time after switch-off of ECRH in case (d), as well as the steady increase of $W_{\rm dia}$ up to 3.75 s in case (e), are caused by an increase of the density (see figure 9(*b*)) as predicted by the RI-mode scaling law, equation (1) and figure 4. Note that in case (e) density control was lost, leading to a roll-over to low confinement at 3.75 s. In case (e) the central density was above cut-off; therefore, ECRH did not contribute to the energy content in this case. Note the strong reduction of the H_α signal in the RI-mode, as compared to the L-mode, indicative of reduced particle transport; during ECRH the H_α rises, both in L- and RI-modes.

In figure 10 $T_{\rm e}$ and $n_{\rm e}$ profiles from TS from the same five discharges are plotted (the profiles are taken just before the end of the ECRH pulse). With increasing neon content the $n_{\rm e}$ profile is seen to peak, whereas the $T_{\rm e}$ profile hardly changes. This peaking of $n_{\rm e}$ is reflected in the increasing $W_{\rm dia}$ (figure 9(*c*)) with increasing neon puff (neon-VIII signal shown in the upper panel of figure 9).

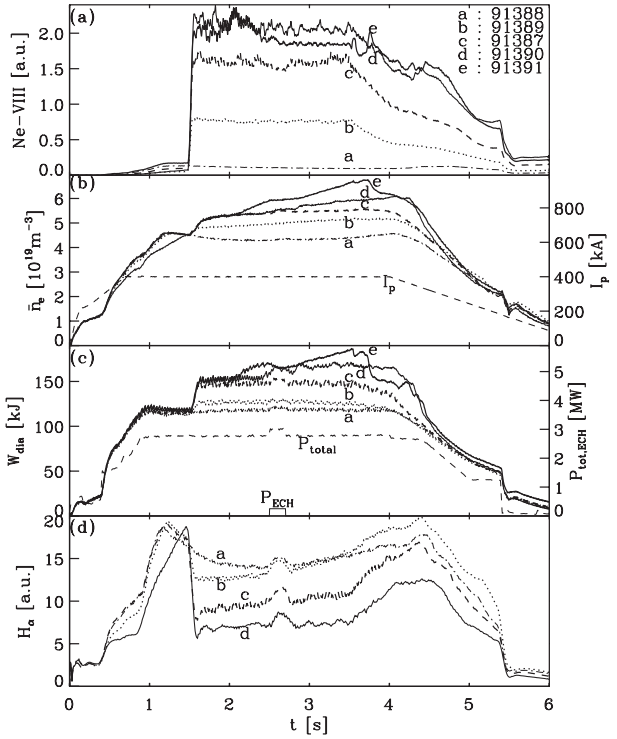

Figure 9. Time traces of five TEXTOR similar discharges with increasing neon puff, indicated with the letters a, b, c, d, e in the plot. Neon puff in arbitrary units (*a*), $n_{\rm e}$ and $I_{\rm p}$ (*b*), $W_{\rm dia}$, total input power and $P_{\rm ECRH}$ (*c*), and H_α signal (*d*) are shown.

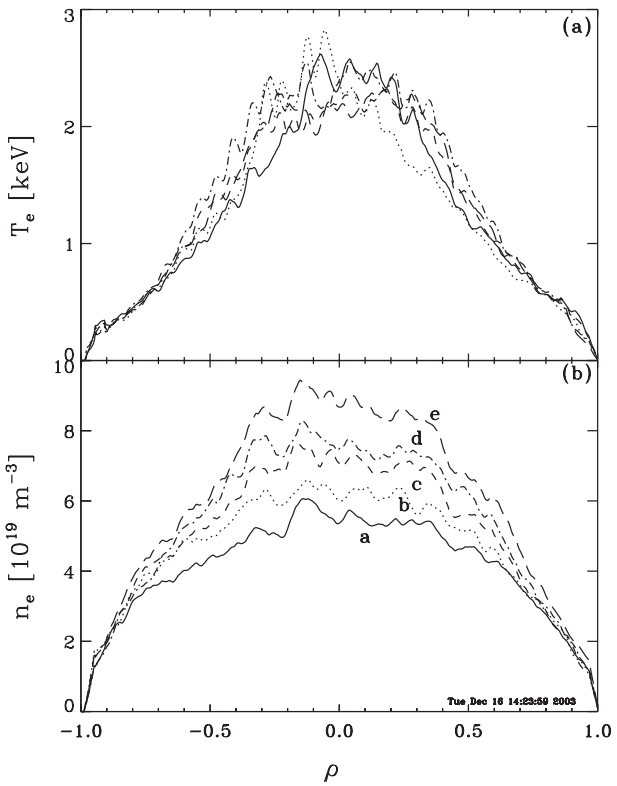

Figure 10. Profiles of $T_{\rm e}$ (*a*) and $n_{\rm e}$ (*b*) from TS, for the same five discharges and in the same line coding as in figure 9. With increasing neon content the $n_{\rm e}$ profile is seen to peak, whereas the $T_{\rm e}$ profile hardly changes.

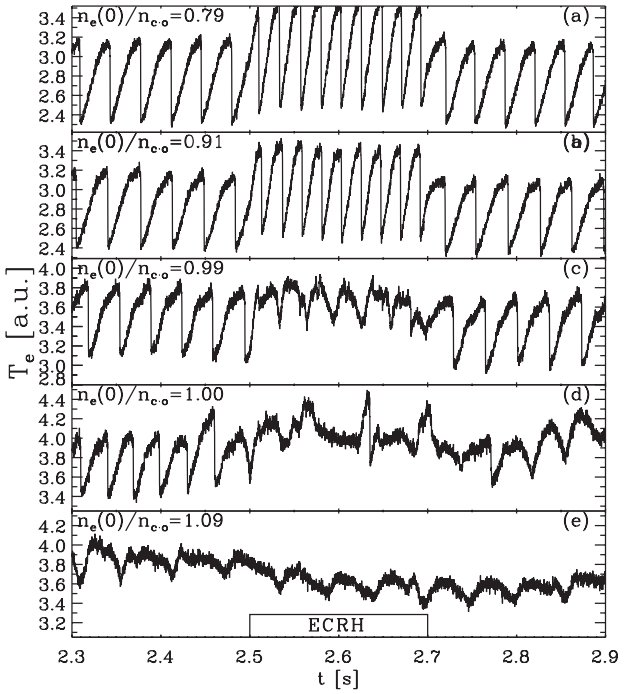

Figure 11. Third harmonic ECE time traces, coming from the centre of the plasma, for the five discharges of figure 9. For each curve $n_e(0)/n_{c.o.}^{110,X}$ at the start of the ECRH pulse is given. The same arbitrary units were used in all panels.

The change in sawtooth behaviour in this scan is striking. This can already be seen on some time traces in figure 9, but is much more clearly documented by the third harmonic ECE signals in figure 11 (the second harmonic ECE, normally used for T_e measurement, is in cut-off). The sawtooth behaviour changes from normal to humpback-like at the highest neon puff level, i.e. at the highest density (case e); interestingly, ECRH appears to trigger a similar change already at somewhat lower densities (cases c and d). It should be noted that this ECRH related sawtooth change occurs in cases where $n_e(0)$ is close to $n_{c.o.}^{110,X}$, so it might be related to off-axis heating due to refraction of the ECRH beam.

Figure 12 further documents the effect of ECRH on the sawteeth as a function of density: it shows the central third harmonic ECE for three different discharges: from bottom to top, a discharge at moderate density showing normal sawteeth with decrease of sawtooth period (τ_{st}) during central ECRH, a discharge close to $n_{c.o.}^{110,X}$ showing first the short period normal sawteeth changing into humpback-like towards the end of the ECRH pulse, and finally a discharge just above $n_{c.o.}^{110,X}$ in which practically no effect of ECRH can be seen. The change of sawtooth behaviour from normal to humpback-like is also observed within discharges with a slow density ramp-up during the RI-mode (see figure 13).

Finally, it should be noted that ECRH decreases τ_{st} only for $\rho_{dep} \lessapprox \rho_{inv}$, as is documented in figure 14, where τ_{st} during ECRH is given, normalized to τ_{st} without ECRH in the same discharge. In discharges with off-axis ECRH as the only external heating source, τ_{st} is increased or the sawteeth are even stabilized when ρ_{dep} is just outside ρ_{inv} [15]. In the discharges presented here, however, the contribution of ECRH to the total power is too small to have this effect.

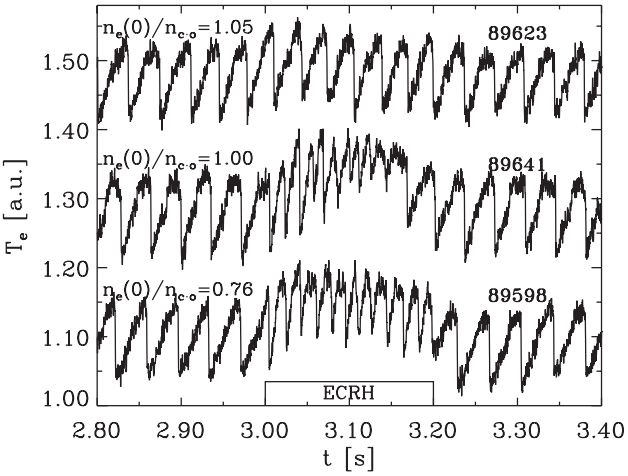

Figure 12. The sawtooth behaviour during central ECRH in the RI-mode at different densities. Discharge numbers and $n_e(0)/n_{c.o.}^{110,X}$ are given in the plot. The density increases from well below cut-off for the discharge displayed in the bottom trace to above cut-off for the top trace. The middle trace showing a transition to humpback-like sawteeth during ECRH is for a case close to cut-off.

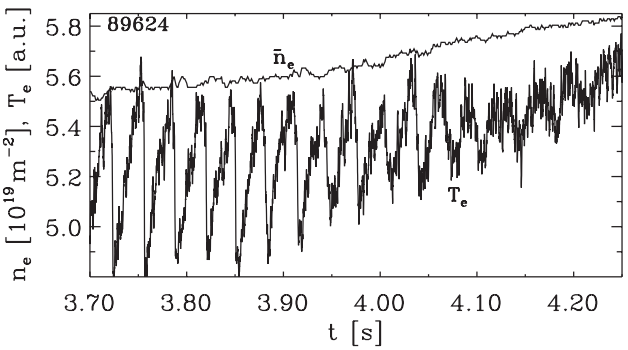

Figure 13. The sawtooth behaviour in a standard RI-mode discharge measured with third harmonic X-mode ECE. With increasing density, the sawtooth behaviour changes from normal to humpback-like. Note that the changeover occurs at a density just above the 110 GHz X-mode cut-off.

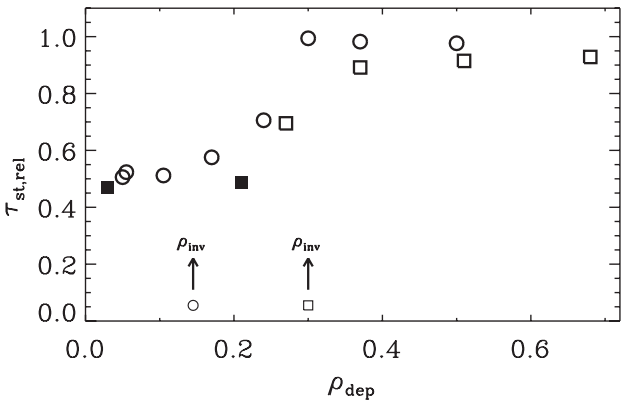

Figure 14. Effect of ECRH on the sawtooth period (τ_{st}) as function of ρ_{dep} for the dataset of figure 8. The plot shows τ_{st} during ECRH normalized to τ_{st} in the same discharge during the RI-mode phase before the start of ECRH. Closed symbols are cases where the sawteeth become of compound character during ECRH.

7. Discussion

When one wants to understand turbulent transport mechanisms in the L-mode and RI-mode, it is useful to look at the scale lengths of the q, n_e, T_e and T_i profiles, defined as $L_q = q/|\nabla q|$, $L_n = n/|\nabla n|$ and $L_{T_{e,i}} = T_{e,i}/|\nabla T_{e,i}|$. In the following, we consider the dimensionless inverse scale lengths, defined as $\Pi_n = a/L_n$ and $\Pi_{T_{e,i}} = a/L_{T_{e,i}}$, to characterize the peaking of the n_e, T_e and T_i profiles; moreover Π_{rel} is defined as Π_n/Π_{T_i}, i.e. the peaking of n_e relative to T_i.

The transition from L-mode to RI-mode is believed to be caused by suppression of ITG modes [7]. Following the modelling of [7], the maximum growth rate of the ITG mode (γ_{ITG}^{max}), on the one hand, increases with T_e and Π_{T_i} and, on the other hand, decreases with Z_{eff} and Π_{rel}. The suppression mechanism is as follows: Z_{eff} is increased by neon puffing; this decreases γ_{ITG}^{max}, which leads to peaking of n_e, which in turn further decreases γ_{ITG}^{max}. In the end this leads to full suppression of the ITG mode, which is achieved if [7]

$$\Pi_n \geqslant \Pi_{n,crit}^{ITG} = 4\left(\sqrt{\frac{0.67^2}{Z_{eff}^2} + \frac{\Pi_{T_i}}{2Z_{eff}}} - \frac{0.67}{Z_{eff}}\right) \qquad (3)$$

This expression is only valid for relatively steep n_e profiles, as typical for TEXTOR; moreover, the dependence on T_e/T_i is not taken into account in this expression.

It should be noted that a strong reduction of density and potential fluctuations near the edge of the RI-mode discharges was indeed observed, as compared to the L-mode; the associated radial turbulent particle flux was reduced by a factor of about 4–7 [16]. Also in DIII-D reduction of long-wavelength turbulence was observed after impurity injection [17].

Once ITG turbulence is quenched, dissipative trapped electron (DTE) modes are considered as the most important transport mechanism. DTE turbulence also produces a strong inward particle convection, with

$$V^{DTE} = -\frac{D^{DTE}}{L_q} \qquad (4)$$

with V, D being the particle convection velocity and particle diffusion coefficient [7], thus maintaining the peaked density profile.

Let us now consider the changes ECRH brings to the plasma. In the L-mode the ITG mode is further enhanced when T_e increases, so heating with ECRH is expected to further deteriorate confinement, in accordance with the experimental observation in TEXTOR (not shown here) that ECR heating in the L-mode obeys standard power degradation ($\tau_E \sim P_{tot}^{-2/3}$). On the other hand, $\Pi_{n,crit}^{ITG}$ does not depend on T_e or Π_{T_e}, so once ITG has been suppressed, the T_e profile is allowed to peak without destabilizing the ITG modes. This at least qualitatively explains the effectiveness of ECRH in RI-mode plasmas. Moreover, the n_e profile shape in the RI-mode is governed by DTE, i.e. by L_q (see equation (4)), so no density flattening is expected during ECRH, in contrast to the situation in the L-mode (so-called density pump-out, a common observation when ECRH is applied).

To make this discussion somewhat more concrete, we have calculated Π_n and $\Pi_n/\Pi_{n,crit}^{ITG}$ for the four discharges of figure 5(*a*) (see figures 15(*a*) and (*b*)). Indeed, it is seen that in the L-mode case (thin lines) $\Pi_n/\Pi_{n,crit}^{ITG} < 1$ over most of the cross-section, i.e. the peaking of n_e is too low to suppress ITG modes. On the other hand, in the RI-mode (thick lines) $\Pi_n/\Pi_{n,crit}^{ITG} > 1$ for a good part of the cross-section. So one could conclude that, at least for these specific discharges, ITG is suppressed in the RI-mode and that ECRH has no deteriorating effect.

Increased peaking of T_e could destabilize short wavelength electron temperature gradient (ETG) modes, so this could put

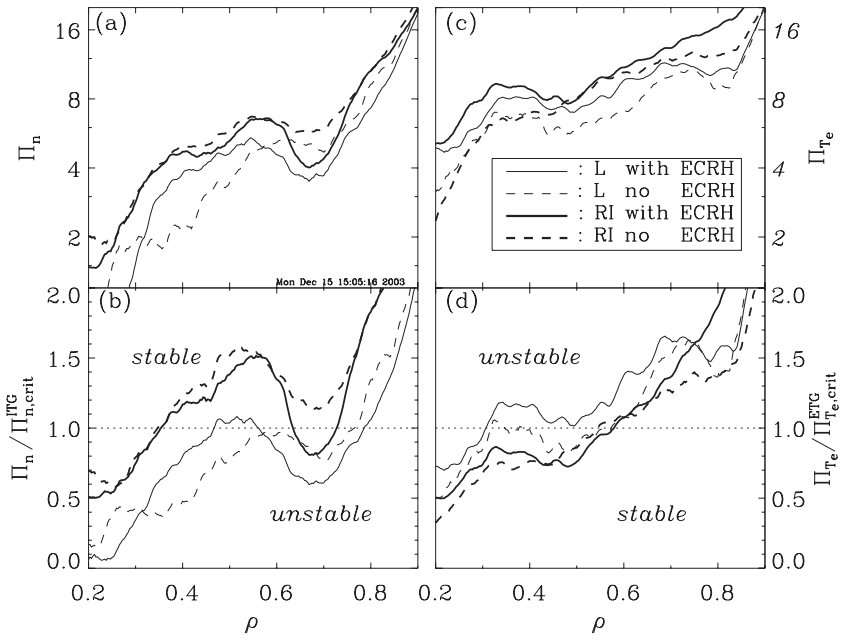

Figure 15. Profiles of Π_n (*a*), $\Pi_n/\Pi_{n,crit}^{ITG}$ (*b*), Π_{T_e} (*c*) and $\Pi_{T_e}/\Pi_{T_e,crit}^{ETG}$ (*d*) for the four discharges of figure 5(*a*), with the same line coding (see section 7).

an end to the effective heating with ECRH. Several expressions exist for critical ∇T_e above which ETG modes are excited. Here, we follow [18]: ETG is excited if

$$\Pi_{T_e} \geqslant \Pi^{\mathrm{ETG}}_{T_{e,\mathrm{crit}}} = (1+\tau)\left(\mathcal{A} + \frac{\mathcal{B}s}{q}\right) f(\epsilon) \qquad (5)$$

where $\tau = Z_{\mathrm{eff}} T_e / T_i$, $\mathcal{A} = 1.33$, $\mathcal{B} = 1.91$, s is the magnetic shear and f is a function of the inverse aspect ratio ($\epsilon = r/R$) of order unity. Figure 15(c) shows Π_{T_e} and figure 15(d) shows $\Pi_{T_e}/\Pi^{\mathrm{ETG}}_{T_{e,\mathrm{crit}}}$ for the same four discharges as before. It should be noted that there are quite large uncertainties in the $\Pi^{\mathrm{ETG}}_{T_{e,\mathrm{crit}}}$ profiles presented here, mainly due to uncertainties in T_i, q and s. The q profiles used here were calculated from the T_e profiles taking into account the neoclassical correction and bootstrap current. For the L-mode cases Z_{eff} was assumed to be flat; for the RI-mode cases a Z_{eff} profile with $Z_{\mathrm{eff}}(a) = 2Z_{\mathrm{eff}}(0)$ was taken, as is typical for RI-mode discharges.

With these uncertainties in mind one can tentatively say that in the RI-mode discharge without ECRH (thick dashed line) Π_{T_e} is clearly below $\Pi^{\mathrm{ETG}}_{T_{e,\mathrm{crit}}}$ inside $\rho \sim 0.5$, and that this is still true with ECRH (thick full line) in spite of the peaking of T_e. There even appears to be room for further peaking of T_e inside $\rho \sim 0.5$. These results appear to indicate that in RI-mode discharges the T_e profile is non-stiff (stiff) inside (outside) $\rho \sim 0.5$, whereas in L-mode discharges the non-stiff region is limited to the very centre. This is in agreement with the observed profiles (see, e.g. figure 5(a)) it is also in agreement with the results of the power deposition scans (figure 8). Note that in the edge region, for $\rho \gtrapprox 0.7$, the T_e profile is strongly affected by radiation losses and no longer governed by turbulence alone. The feature that Π_{T_e} is below $\Pi^{\mathrm{ETG}}_{T_{e,\mathrm{crit}}}$ in the inner part and above $\Pi^{\mathrm{ETG}}_{T_{e,\mathrm{crit}}}$ close to the edge was also observed in Tore Supra [19].

8. Conclusions and outlook

In spite of the modest level and duration of the current ECRH power very interesting results have been obtained, in terms of performance improvement (compared to standard scaling laws) and change of sawtooth behaviour (reduction of τ_{st} for $n_e(0) < n^{110,\mathrm{X}}_{\mathrm{c.o.}}$; change from normal to humpback-like sawteeth for $n_e(0) \simeq n^{110,\mathrm{X}}_{\mathrm{c.o.}}$).

Up to the ECRH X-mode cut-off density, the energy content of RI-mode discharges can be increased with ECRH without power degradation. It appears that in the RI-mode with ECRH the T_e profile can be peaked without increasing turbulent transport. This is confirmed by some comparisons with simple model calculations. The effectiveness of ECRH sharply decreases when the power deposition is moved outside ρ_{inv}.

In contrast to L-mode discharges, no density pump-out is observed when ECRH is used in RI-mode discharges; only a slight flattening of the n_e profile is seen. The toroidal rotation slows down significantly during ECRH, both in the L- and RI-modes; the cause of this is unknown.

When operations of TEXTOR restart after the 2001–2003 shut-down, a new gyrotron (140 GHz, 1 MW, 3–10 s) will be available [20]. This long-pulse high-power gyrotron will allow a very significant extension of the study of electron heat transport in RI-mode discharges. First, the increased cut-off frequency at 140 GHz will allow effective heating also in the highest performance RI-mode discharges. Second, with the new gyrotron, a significant fraction of input power can be delivered (∼30% instead of ∼10%); if the increase of stored energy were to still scale linearly with input power, then a significant enhancement over the RI-mode scaling could be achieved, and this would shed more light on the turbulence suppression mechanisms in the RI-mode. Third, the higher power of the new gyrotron will allow us to perform on- and off-axis power modulation studies also in the RI-mode. In particular, the pulse length of several seconds will allow us to apply modulated ECRH across the transition from the L-mode to the RI-mode, to probe local changes in electron thermal transport.

Acknowledgments

This work, supported by the European Communities under the contract of Association between EURATOM/FOM, was carried out within the framework of the European Fusion Programme with financial support from NWO. The views and opinions expressed herein do not necessarily reflect those of the European Commission.

References

[1] Weynants R.R. *et al* 1999 *Nucl. Fusion* **39** 1637
[2] Ongena J. *et al* 1999 *Plasma Phys. Control. Fusion* **41** A379
[3] Jackson G.L. *et al* 2002 *Plasma Phys. Control. Fusion* **44** 1893
[4] Dumortier P. *et al* 2002 *Plasma Phys. Control. Fusion* **44** 1845
[5] Tokar M.Z. *et al* 2002 *Plasma Phys. Control. Fusion* **44** 1903
[6] Frigione D. *et al* 2002 *29th EPS Conf. (Montreux)* vol 26B (Geneva: EPS) CD-ROM, paper P-2.053
[7] Tokar M.Z. *et al* 2000 *Phys. Rev. Lett.* **84** 895
[8] Kreter A. *et al* 2003 *Plasma Phys. Control. Fusion* **44** 199
[9] Kalupin D. *et al* 2001 *Plasma Phys. Control. Fusion* **43** 945
[10] Kaye S.M. *et al* 1997 *Nucl. Fusion* **37** 1303
[11] Westerhof E. 1989 Implementation of TORAY at JET *Rijnhuizen Report* pp 89–183
[12] Sillen R.M.J. *et al* 1986 NOTEC, a code to simulate electron cyclotron emission spectra of plasmas which include non-thermal populations *Rijnhuizen Report* pp 86–165
[13] deGrassie J.S. *et al* 1999 *26th EPS Conf. (Maastricht)* vol 23J (Geneva: EPS) p 1189
[14] Eriksson L.G. *et al* 1993 *Nucl. Fusion* **33** 1037
[15] Jaspers R.J.E. *et al* 2002 *29th EPS Conf. (Montreux)* vol 26B (Geneva: EPS) CD-ROM, paper P-2.063
[16] Boedo J.A. *et al* 2000 *Nucl. Fusion* **40** 209
[17] Murakami M. *et al* 2001 *Nucl. Fusion* **41** 317
[18] Jenko F. *et al* 2001 *Phys. Plasmas* **8** 4096
[19] Jenko F. *et al* 2002 *Phys. Rev. Lett.* **89** 225001
[20] Hoekzema J.A. *et al* 2002 The 140 GHz ECW system on Textor *Proc. 12th Joint Workshop on ECE and ECRH (Aix-en-Provence, France)* (Singapore: World Scientific) p 541